Lanthanide-directed metal–organic coordination networks

Sofia O. Parreiras, José M. Gallego, David Écija

ARTICLE

Lanthanide-directed metal-organic coordination networks

Sofia O. Parreiras,[a] José M. Gallego,*[b] and David Écija*[a]

The synthesis of two-dimensional metal-organic networks (2D-MOCNs) on solid substrates is a rapidly growing field of research due to their potential applications in gas sensing, catalysis, energy storage, spintronics, and quantum information. In addition, the possibility of using lanthanides as coordination nodes makes them a very straightforward alternative to create an ordered array of magnetic atoms on a surface, thus paving the way for their use in information storage at the single-atom level. This feature article reviews the strategies to design two-dimensional periodic nanoarchitectures comprising lanthanide atoms in ultra-high vacuum (UHV) environment, focusing on lanthanide-directed 2D-MOCNs on metal surfaces and decoupling substrates. The characterization of their structure, electronic, and magnetic properties is also discussed, including the use of state-of-the-art scanning probe microscopies and photoelectron spectroscopies, complemented by Density Functional Theory calculations and multiplet simulations.

Contents

Introduction

Since the discovery of magnetic remanence below 4 K in the coordination compound Mn12-Ac,[1] single molecule magnets (SMMs) have been considered a realistic viable alternative for ultra-high density magnetic storage, due to their potential to reduce the size of the information bit to a few angstroms. An important step in this direction was the report of a similar SMM behaviour in single-ion lanthanide double-deckers.[2] In addition, magnetic molecules have also been proposed as candidates for the implementation of qubits for quantum information processing (QIP).[3]

The integration of SMMs in actual storage devices requires the capability of creating an ordered array of SMMs on a solid substrate with no detrimental of their magnetic properties. While significant progress has been made in the last decades,[4,5] this manuscript reviews an alternative approach for creating an ordered array of magnetic atoms, particularly the coordination of lanthanide elements with molecular linkers on a solid surface. Such strategy involves using on-surface synthesis methods to fabricate two-dimensional lanthanide-directed metal-organic networks.

The article's structure is as follows: firstly, we will provide a brief explanation of how a SMM works, with a particular emphasis on lanthanide-based SMMs that currently appear to be the most promising. Then, we will discuss the fabrication of an ordered array of lanthanides on a solid surface. Finally, we will present the most relevant results regarding the growth and properties of 2D lanthanide-based metal-organic networks. Such strategy could be considered one of the most direct ways of creating an ordered array of lanthanide atoms or clusters on a solid surface, which is a necessary prerequisite for their use in electronic or magnetic devices.

There are many excellent books and reviews about the electronic and magnetic properties of lanthanide elements and their compounds, which will be revisited in this review. For general references to this introduction, see Refs. [4–12]

Molecular magnets: how do they work?

SMMs are metal-organic or organometallic compounds that display strong magnetic anisotropy and therefore are able to exhibit magnetic remanence below the so-called blocking temperature. When a magnetic field is applied along the easy axis direction, the unpaired spins of the compound align with

[a] Instituto Madrileño de Estudios Avanzados en Nanociencia (IMDEA Nanoscience). 28049-Madrid, Spain. E-mail: david.ecija@imdea.org
[b] Instituto de Ciencia de Materiales de Madrid (ICMM), CSIC, 28049-Madrid, Spain. E-mail: josemaria.gallego@csic.es

the direction of the field. However, when the field is removed, the spins are able to maintain their orientation for a certain period of time, and the system shows a non-zero magnetic remanence.

A SMM must fulfill the following requirements: i) the existence of a bistable ground state, provided by a uniaxial magnetic anisotropy, with a large $\pm M_J$ quantum number to ensure a ground state with a large magnetic moment; and ii) a large energy barrier for spin reversal between the two states, since the larger the energy barrier, a longer time and at higher temperatures can the spins maintain their orientation.

Mn12-ac, the first discovered SMM, is a coordination compound containing 12 metallic centers, four Mn^{4+} and eight Mn^{3+} ions. The antiferromagnetic interaction between them gives rise to a ground state with a spin value of S = 10, which is 21-fold degenerate ($M_S = 2S + 1$). However, due to the zero-field splitting (ZFS), which fundamentally depends on the axial anisotropy of the ground state, the 21 sublevels are separated, their energy given now by $E(M_S) = M_S^2 D$, (where D is the axial anisotropy parameter). When D < 0 (easy axis anisotropy), the

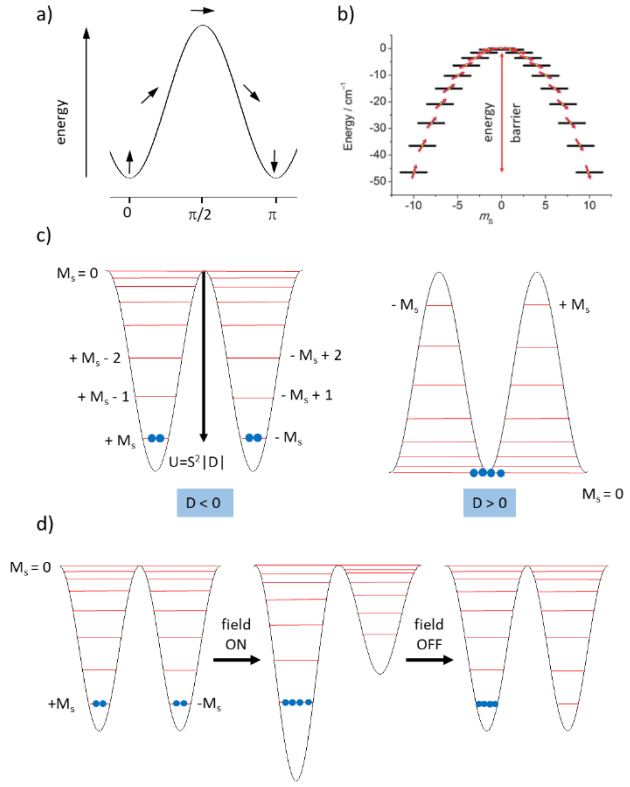

Figure 1. a) Energy of an Ising type magnet as a function of the angle of the magnetization from the easy axis. b) Potential energy as a function of the M_J quantum number calculated for Mn12-ac. Reproduced from Ref. [123] with permission from the Royal Society of Chemistry. c) Double-well energy diagram for negative (left) and positive (right) values of axial anisotropy, D. Adapted from Ref. [18] with permission from the Royal Society of Chemistry. d) Schematic diagram showing the magnetization and magnetic relaxation processes in a single molecular magnet before and after applying an external magnetic field. Reproduced from Ref. [16] with permission from the Royal Society of Chemistry.

low-lying energy levels are the ones with highest $|M_S|$ value, in this case $M_S = \pm 10$ (Figure 2c, left). The magnetization associated to each of the $M_S = \pm 10$ sublevels has its particular orientation along the axial anisotropy axis, whereby $M_S = +10$ stands for spin up and $M_S = -10$ stands for spin down. However, when D > 0 (easy plane anisotropy), the opposite situation is given, so that the ground state would be $M_S = 0$, there is not any possibility for a bistable ground state and, hence, the system is not valid for information storage (Figure 2c, right). Coming back to the first situation (D < 0), in order to switch or have an inversion of the magnetization from $M_S = +10$ to $M_S = -10$, the system needs to overcome an energy barrier, U (see Figure 1). The value of the barrier is the difference between the highest excited state and the ground state. For systems with integer and non-integer spin values it is defined as $U = S^2|D|$ and $U = S^2 - 1/4|D|$, respectively (S being the spin value of the ground state).

In the absence of an external magnetic field the two $M_S = \pm 10$ sublevels have the same energy and are equally populated, thus the system does not present any magnetization (Figure 2d, left). When an external magnetic field of enough intensity is applied in a certain direction, one of the M_S sublevels is stabilized in comparison to the other. Therefore, the material shows a magnetization, since the spin of all the molecules point out in the same direction (Figure 2d, middle). When the magnetic field is removed, the ground state reaches again a doubly degenerate state, and if $E_T > U$, the material will tend to achieve the equilibrium between the two orientations (positive and negative), losing magnetization. Nonetheless, if $E_T < U$, which is the situation that occurs when $T < T_B$ (T_B is the blocking temperature), the magnetization will be blocked and that is why SMMs are able to store information (Figure 2d, right). Thus, in principle, the larger the energy barrier, the larger will be the temperature at which the magnetization can be retained.

Due to the quantum nature of these materials, there are different relaxation processes, such as those that occur through spin-phonon coupling (direct, that involves only one phonon

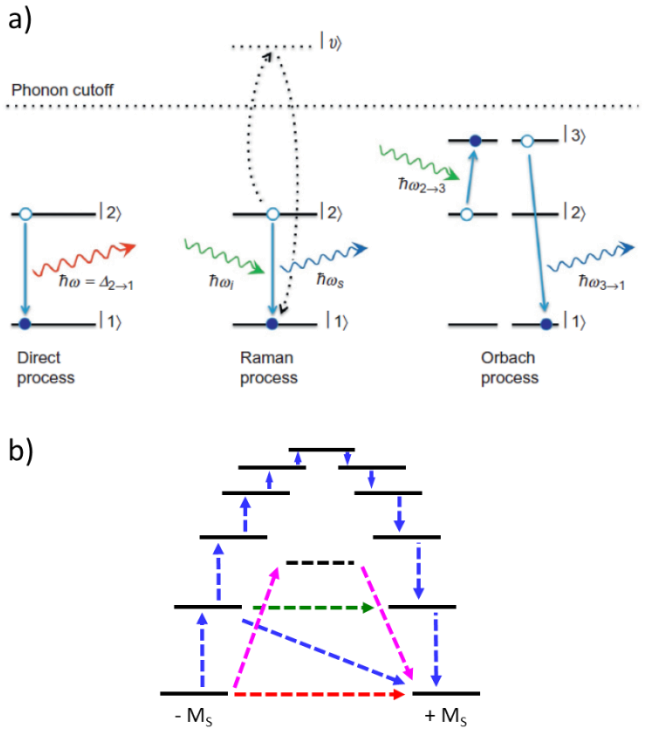

Figure 2. a) Level scheme for spin–lattice relaxation processes: Direct, Raman, and Orbach processes. Reproduced from Ref. [124] with permission from Copyright © 2017 Elsevier. b) The most common mechanisms involved in the magnetization relaxation of magnetically bi-stable systems. Colour codes: blue = thermally activated (Orbach) process; red = quantum tunnelling of magnetization (QTM); green = thermally assisted (TA) QTM; pink = Raman process. The black horizontal dashed line indicates a virtual state.

process, and Orbach and Raman, that are two phonon processes) or the ones that happen due to the quantum nature of the materials (Quantum Tunnelling of the Magnetization, QTM, and Thermally Assisted QTM, TA-QTM) (Figure 2).[4,13] An ideal Orbach relaxation would be the one in which the system overcomes the entire barrier, but more often occurs through the first or second excited state.

Their net effect is the decrease of the barrier U, giving rise to an effective energy barrier, U_{eff}. Concomitantly, there is a variation of the blocking temperature and the relaxation time. In particular, since the relaxation process often takes place through the first excited state, it is important that, besides a ground state with the highest possible absolute value of M_J, which could be accomplished when the anisotropy of the ground state is uniaxial, the energetic separation between M_J and $M_J \pm 1$ states should be as high as possible. In addition, it has been shown that the minimization of transverse (i.e., perpendicular to the magnetic anisotropy axis) crystal fields reduce the mixing between different M_J states and suppress the quantum tunneling of magnetization (QTM).[14,15]

Since the energy barrier goes as $U = DS^2$, the first attempts to increase the so-called blocking temperature were directed at increasing the total spin S of the molecular complex by augmenting the number of metal ions. However, it soon became very clear that this approach did not work as expected, especially since it was shown that $D \propto 1/S^2$, so U is, in a first approximation, independent of S.[16] This led to a completely new approach, where the focus was to find simpler systems with a large uniaxial anisotropy instead of complex polynuclear compounds.[2] The research shifted then to the so-called single-ion magnets (SIMs), where the magnetic atom could either be a 3d transition metal [17,18] or a lanthanide element,[2,5] each option having their own pros and cons: while lanthanide elements have a strong magnetic anisotropy and higher magnetic moments, 3D systems have the ability to create strongly coupled spin systems.[4,18] However, lanthanide-based SMMs took a big step forward with the synthesis of a metallocene compound that could hold up the magnetic bistability up to 60 K,[19,20] and this was soon followed by the discovery of another compound with a blocking temperature above the iconic liquid-nitrogen temperature.[21]

	Ln^0	Ln^{III}	L	S	J		g_J	μ
La	[Xe] $5d^16s^2$	[Xe]	0	0	0	$^1S_0$		0.00
Ce	[Xe] $4f^15d^16s^2$	[Xe] $4f^1$	3	1/2	5/2	$^2F_{5/2}$	6/7	2.54
Pr	[Xe] $4f^36s^2$	[Xe] $4f^2$	5	1	4	$^3H_4$	4/5	3.58
Nd	[Xe] $4f^46s^2$	[Xe] $4f^3$	6	3/2	9/2	$^4I_{9/2}$	8/11	3.62
Pm	[Xe] $4f^56s^2$	[Xe] $4f^4$	6	2	4	$^5I_4$	3/5	2.68
Sm	[Xe] $4f^66s^2$	[Xe] $4f^5$	5	5/2	5/2	$^6H_{5/2}$	2/7	0.85
Eu	[Xe] $4f^76s^2$	[Xe] $4f^6$	3	3	0	$^7F_0$		0.00
Gd	[Xe] $4f^75d^16s^2$	[Xe] $4f^7$	0	7/2	7/2	$^8S_{7/2}$	2	7.94
Tb	[Xe] $4f^96s^2$	[Xe] $4f^8$	3	3	6	$^7F_6$	3/2	9.72
Dy	[Xe] $4f^{10}6s^2$	[Xe] $4f^9$	5	5/2	15/2	$^6H_{15/2}$	4/3	10.65
Ho	[Xe] $4f^{11}6s^2$	[Xe] $4f^{10}$	6	2	8	$^5I_8$	5/4	10.61
Er	[Xe] $4f^{12}6s^2$	[Xe] $4f^{11}$	6	3/2	15/2	$^4I_{15/2}$	6/5	9.58
Tm	[Xe] $4f^{13}6s^2$	[Xe] $4f^{12}$	5	1	6	$^3H_6$	7/6	7.56
Yb	[Xe] $4f^{14}6s^2$	[Xe] $4f^{13}$	3	1/2	7/2	$^2F_{7/2}$	8/7	4.54
Lu	[Xe] $4f^{14}5d^16s^2$	[Xe] $4f^{14}$	0	0	0	$^1S_0$		0.00

Table 1. Electronic structure of the rare-earth elements in neutral and +3 oxidation state. The associated L, S, and J quantum numbers, spectroscopic term, g_J factor, and magnetic moment (calculated from Equation (1), in units of μ_B) refer to the +3 ions.

This review focuses on rare-earth elements and their surface-confined metal-organic complexes and networks.

The electronic structure of rare-earth elements

The strongest magnets known to date, such as $SmCo_5$ and $Nd_2Fe_{14}B$, are alloys based on lanthanides, due to their high magnetic moment and high magnetic anisotropy.

In their metallic form (Ln^0), lanthanides are characterized by the progressive filling of the 4f shell, with an electronic configuration of the type $[Xe]6s^24f^{n+1}$. Lanthanum, cerium, gadolinium, and lutetium are the exceptions, with one 5d orbital also occupied by one electron (see Table 1). The most common oxidation state is +3, with an electronic configuration of $[Xe]4f^n$ for all the ions. Nonetheless, europium and ytterbium are quite commonly found in an oxidation state of +2,[22,23] and cerium and terbium in an oxidation state of +4, the reason being the extra stability attained by the empty, half-filled or fully filled f shell.

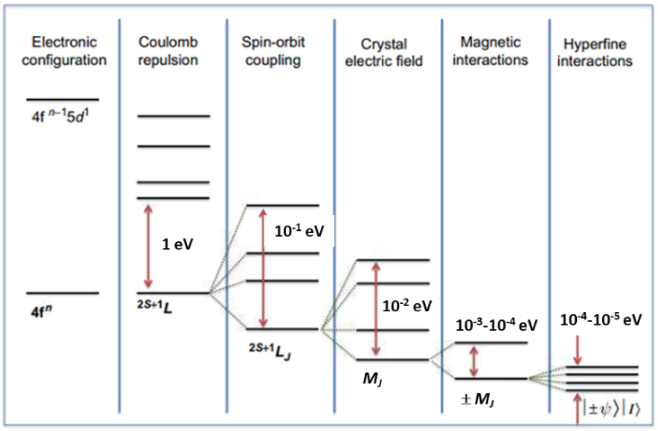

Figure 3. Schematic electronic structure of a lanthanide ion. Adapted from Ref. [124] with permission from Copyright © 2017 Elsevier.

The 4f electrons are very localized and are effectively shielded from the environment by the $5s^2$ and $5p^6$ electrons, and thus their contribution to the bonding is minor. As a result, while the 4f electrons are the responsible for the magnetic properties, the physical and chemical properties are in general dictated by the 5d and 6s valence electrons, which are the major contributors to bonding.

Shielding of the 4f electrons implies that the orbital angular momentum remains mostly unquenched by crystal fields, resulting in a significantly strong spin-orbit coupling. As a result, considering that the spin–orbit coupling is the main source of magnetic anisotropy, in principle, the magnetic anisotropy value will usually be higher for lanthanides than for transition metal complexes.

Importantly, due to such strong spin-orbit coupling, the magnetic properties of lanthanides will be now described by using the Russell–Saunders coupling scheme. The magnetic moments are given by the expression

$$\mu = g_J[J((J+1)]^{1/2} \quad (1)$$

where

$$g_J = 1 + \left[\frac{S(S+1)+J(J+1)-L(L+1)}{2J(J+1)}\right]$$

with $J = (L + S)$ for a shell more than half-filled and $J = (L - S)$ for a shell less than half-filled.

In general, a strong spin–orbit coupling means that the excited states are well above the ground state, so that the properties of the ground state are usually an accurate representation of the magnetic behavior of lanthanide ions. All paramagnetic lanthanide ions (except Gd^{3+} and Eu^{2+}, with half-filled shell f^7 electron configuration), have orbitally degenerated ground states. For a $4f^7$ lanthanide ion such as Gd^{3+}, the contribution to its magnetic behavior is only from a pure spin state $S = 7/2$. For a lanthanide ion with $4f^n$ $(n \neq 7)$ configuration, the ground state energy is split by electronic repulsion in spectroscopic terms, the one with the highest spin multiplicity $(2S + 1)$ being the lowest in energy, limited by Hund's rule of maximum spin multiplicity. Each of these terms is further split by the spin–orbit interaction into $^{2S+1}L_J$ spectroscopic levels, with $|L - S| \leq J \leq L + S$. The corresponding energy spectrum of these states can be calculated as

$$E(^{2S+1}L_J) = \left(\frac{\lambda}{2}\right)[J(J+1) - L(L+1) - S(S+1)],$$

where λ is the spin-orbit coupling constant. Each of these levels can be further split into Stark sublevels (that are described by M_J) by the ligand field. The splitting structure in sublevels by the progressively weaker interactions is schematically represented in Figure 3.

This subordination of the crystal field to the spin–orbit interaction makes it a minor factor in the overall electronic structure, yet it turns out to be a key factor in creating single-molecule magnets with f-elements. The interaction of the ground spin–orbit coupled J state with the crystal field generates the magnetic anisotropy barrier separating opposite orientations of the spin ground state. As a result of such magnetic anisotropy, the energetically split electronic states have different magnetic properties, for example different directions of the magnetic moment. Notably, due to the shielding of the 4f orbitals, the ligand field splitting is much smaller than for the 3d orbitals of the transition metal ions.

Following quantum mechanical considerations, for odd-numbered electronic configurations (e.g. Dy^{3+}, Er^{3+}, Yb^{3+}), the electric field generated by the ligands does not completely lift the degeneracy of $^{2S+1}L_J$ levels, and each Stark sub-level remains at least doubly degenerate (Kramers doublet), a key feature required to observe SMM-type behavior. However, regardless the nature of J, this double degeneracy is lost in the presence of an external magnetic field, which is the Zeeman effect. Finally, each of the Zeeman lines can again be split into a set of very closely spaced electronic states owing to coupling with nuclear spins (hyperfine splitting) although, this perturbation is usually very weak.

Coordination chemistry of lanthanides

Lanthanides can be coordinated by ligands, which are small molecules or ions that bind to the central metal ion forming a metal complex. Ligands provide spatially localized, usually negative, charges which interact via the resulting electrostatic fields with the 4f orbitals of the Ln^{3+}) ions (rarely with +2 or +4 ions). Since the 4f orbitals are highly localized, there is almost no overlap with the ligand orbitals, and, as a result, the bonding of metal-organic lanthanide complexes is predominantly of ionic character. The electrostatic metal-ligand interactions are reflected in molecular structures of irregular geometry and varying coordination numbers. In comparison with the 3d metals, lanthanides exhibit a much greater range of coordination numbers in their compounds. Typical values lie between 6 and 12, but with values of 3 and 4 when some bulky groups are used.[10]

SMMs should possess a well-defined doubly-degenerate ground state with the highest possible absolute value of M_J. As the electronic spins constitute time-reversal symmetric quantum eigenstates, each of the electronic states is at least doubly degenerate except under few conditions. For systems

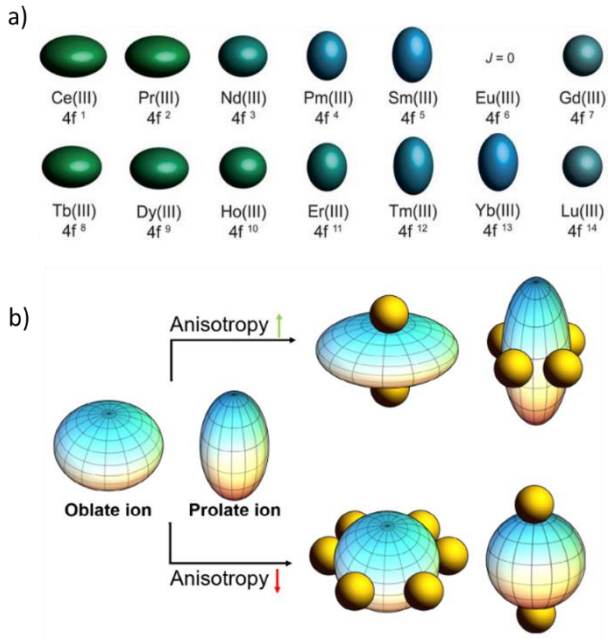

Figure 4. Prolate-oblate coordination model of 4f ions (+3 oxidation state). a) Quadrupole approximations of the 4f-shell electron distribution for the tripositive lanthanides. Reproduced from Ref. [24] with permission from the Royal Society of Chemistry. b) How to enhance or quench the anisotropy for oblate and prolate type of ions. Reproduced from Ref [4] with permission under the terms of the Creative Commons CC BY-NC-ND license.

with an integer value of J, the non-Kramers ions, this double degeneracy of M_J level is lifted in low symmetric environment by the crystal field of the ligands. On the other hand, for systems with a half-integer value of J, the Kramers ions, these factors cannot remove the degeneracy according to the Kramers double degeneracy theorem. Thus, the ground state of Dy^{3+} ions will always be degenerate, irrespective of the ligand field symmetry, while Tb^{3+} ions must have a strictly axial crystal field symmetry to do so. Moreover, the energetic separation between the ground state M_J and the first excited states $M_J \pm 1$ states needs to be as high as possible to obtain high U_{eff} values. These conditions can be facilitated by a rational design of the ligand field. Rinehart and Long proposed some very useful guidelines in this direction based on the analysis of the expected electronic density of the lanthanide cation and its interaction with the crystal field.[24] Among the ions with anisotropic electron density (the Gd^{3+} ion is completely isotropic), two main groups may be distinguished): oblate type ions (Ce^{3+}, Pr^{3+}, Nd^{3+}, Tb^{3+}, Dy^{3+}, and Ho^{3+}), where the ground state with the highest M_J has an oblate distribution of the electronic charge, and prolate type ones (Pm^{3+}, Sm^{3+}, Er^{3+}, Tm^{3+}, and Yb^{3+}), where this distribution is prolate (see Figure 4a).

With the purpose of achieving a large axial magnetic anisotropy (see Figure 4b), for oblate type ions the ligand donor atoms with greatest electron density should coordinate at axial positions. This disposition will cause less electronic repulsion between the oblate electronic density of the lanthanide ion and the ligands donor atoms, stabilizing the ground state with higher M_J values. If no donor ligands are coordinated in the equatorial positions, the electron density will expand along the plane enhancing the axial anisotropy, which is perpendicular to the oblate shaped electron density. Such strategy is successfully exploited for lanthanide double-deckers compounds, which are simply a lanthanide atom sandwiched by porphyrinoid tapes.

Regarding the prolate type of ions, for achieving large axial anisotropy the ligand donor atoms with greatest electron density should coordinate at equatorial positions, minimizing the electronic repulsion with the prolate electronic density of the lanthanide ion. If there are no donor ligands in axial positions, the electron density of the lanthanide metal ion can be expanded along the axial direction, leading to a larger axial anisotropy (which is parallel to the prolate electron density). In summary, for 4f oblate ions the ideal configuration should be a sandwich-type coordination, while ions with prolate charge density should have their anisotropy maximized in an equatorial coordination.[4,24] Two representative complexes would be $[Dy(Cpttt)_2]^{+}$ [19,20] and $Er[N(SiMe_3)_2]_3$, respectively.[25]

This simple model explains why Pc_2Dy (where the oblate ion Dy^{3+} is located in a sandwich-type ligand geometry),[26] show a large uniaxial anisotropy. An example of lanthanide molecular magnets featuring an equatorial coordination are $Ln[N(SiMe_3)_2]_3$ compounds. A comparative study was performed using molecules with Dy^{3+} and Er^{3+} ions.[25] It was observed that this equatorial coordination enhanced the uniaxial anisotropy of Er, while having a detrimental effect on Dy, as predicted by the prolate-oblate coordination model.

However, as mentioned above, the expression of a robust molecular magnet character is more complex. The oblate Dy^{3+} and Tb^{3+} ions are considered as ideal candidates for molecular magnetism when coordinated axially, and they are extensively used in single molecule magnets. One example is the Dy and Tb double-deckers, Pc_2Dy and Tb_2Dy, that are found to have slow relaxation time and uniaxial out-of-plane anisotropy.[2] Dy^{3+} is a Kramers ion, which ensures a bistable ground state, while in the case of the Tb^{3+}, that is not a Kramers ion, the bistability is provided by the effective axial symmetry of the crystal field.[24] Herein, since the difference between the ground and the first states is higher for $TbPc_2$ than for $DyPc_2$, the resulting U_{eff} is higher for $TbPc_2$.[2,24]

In summary, to achieve single ion/molecule magnet character, first a highly anisotropic crystal field environment that matches the electron density distribution of the central ion following the oblate-prolate model described above is crucial to create a large energy splitting between different M_J states and stabilizing the largest $\pm M_J$ states as the ground states. Next, the local symmetry of the coordination environment should be intentionally controlled to minimize the transverse crystal fields, in order to reduce the mixing between different M_J states and, thus, suppressing the quantum tunneling of magnetization (QTM). An alternative approach for minimizing QTM through the ground state is to use a Kramers ion (odd electron count), for which breaking of the M_J degeneracy and thus QTM is formally forbidden in strictly zero-field.

Following these guidelines, since the discovery of the first lanthanide SMM,[2] different breakthroughs have been achieved.[4,13,19,20,27–32] The current state of the art SMMs are

based on Dy metallocenes, with Cp derivatives in axial positions (Cp = cyclopentadienyl anion), which have allowed to reach blocking temperatures above 80 K,[21] and coercive fields higher than 14 T (in this case with two Dy ions).[33]

Ordered arrays of lanthanide atoms on solid surfaces

An essential requisite to incorporate SMMs (or SIMs) in technological devices is the feasibility to place them on a certain surface, [4,34] while maintaining a long range order and keeping intact their magnetic properties. Herein, one of the main concerns is to comprehend how the interaction with the surface could be detrimental for the magnetic properties of the molecular magnet.[35–41] Since the birth of the field, different approaches were followed trying to elucidate the role of the substrate and to achieve the preservation of the magnetic functionalities, using both wet methods or vapour deposition techniques.[34,42–44] In this review, we will restrict to sublimation of species in ultra-high vacuum, which is the cleanest protocol to deposit molecules on a solid surface.

Metal-organic complexes on surfaces

A simple way to create an ordered arrangement of magnetic atoms on a solid surface is to make use of the self-assembly capabilities of molecular species on surfaces. Porphyrins, phthalocyanines and their derivatives, for example, can self-assemble when deposited on some substrates. If these molecules are metallated with a magnetic atom, an ordered array of magnetic centers is created.[45,46] Although in many cases the interaction with the metal substrate can quench the magnetic moment, this can be avoided by insulating layers that decouple the metal atoms from the metal substrate. Up to now, most of these studies have used transition metals, although recently it has been shown that some porphyrins and extended porphyrins can also be metallated with lanthanide atoms (although, due to their larger ionic radii, they are displaced off-axis).[47–51] Their magnetic properties have not yet been explored.

However, soon after the discovery of SMM behaviour in rare-earth double deckers,[2] and following the great amount of work done on porphyrins and phthalocyanines on solid surfaces,[46,52] it was found that the combination of lanthanide atoms and porphyrins usually led to the formation of double decker structures (where the lanthanide atom is sandwiched between two porphyrin molecules). This reaction can take place also on solid substrates, by depositing a beam of lanthanide atoms on a surface precovered with a layer of tetrapyrrole molecules and subsequent annealing.[53–55] In either case, when on the surface the double deckers self-assemble by hydrogen bonds or van der Waals interactions.[40,47,56,57] This usually leads to square lattices with a lattice parameter around 14-20 Å, depending on the functional groups attached to the tetrapyrrolic cores. Although a small coercivity was detected for $TbPc_2$ on HOPG,[36,38,58] on nonmagnetic conducting substrates only vanishing remanence and very narrow hysteresis loops were observed,[59,60] much smaller than in bulk measurements,[61] the most notable exception being explained below.

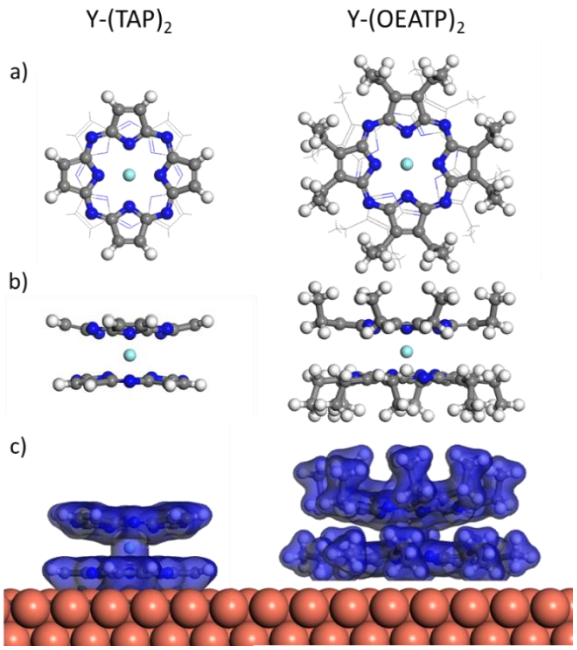

Figure 5. a,b) Top (a) and side (b) views of the gas phase structure of a yttrium-tetraazaphorphyrin double-decker (Y-$(TAP)_2$, left) and a yttrium-octa(ehtyl)tetraazaphorphyrin double-decker (Y-$(OEATP)_2$, right)). b) Charge density isosurface (0.2 $|e^-|$ Å^3) for (a) Y-$(TAP)_2$ on Cu(111) and (b) Y-$(OETAP)_2$ on Cu(111). Adapted from Ref. [62] with permission from the Royal Society of Chemistry.

A simple option to avoid the pernicious influence of the substrate would be to decouple the SMM from the metallic support by a proper choice of the molecular structure.[62] That wisely chosen functional groups in a double (or triple) decker can isolate the rare-earth elements from the substrate influence and is nicely illustrated in Figure 5, which shows the gas-phase configuration, and how it is modified when adsorbed on a Cu(111) surface, of $Y(OETAP)_2$, a double decker functionalized with octaethyl groups, compared to $Y(TAP)_2$. In this way, magnetic hysteresis has been measured on Tb(tbu-Pc)$_2$ islands on Ag(111) at 3 K.[54] This was attributed to the presence of the tert-butyl (tbu) groups attached to the main phthalocyanine structure, that can increase the distance between the magnetic atom and the supporting substrate, reducing the hybridization of the metal ion with the substrate and decoupling it from substrate phonons and electrons.

Another alternative would be to deposit the SMMs on insulating substrates. For example, X-ray magnetic circular dichroism (XMCD) measurements show the opening of hysteresis loops in $TbPc_2$[39] or $DyPc_2$[63] molecules adsorbed on a layer of MgO on Ag(100), but not when the molecules are deposited directly on the bare silver substrate. Density functional theory (DFT) calculations indicate that the hybridization with the substrate orbitals is only slightly larger in the second case, but the analysis of the hysteresis loops point to a much smaller contribution of the two-phonon Raman relaxation process,[63] which is probably related to the smaller

phonon density of states at MgO with respect to the Ag surface.[64] Actually, $TbPc_2$ SMMs on nonmagnetic, insulating MgO on Ag(100) demonstrate record values of the magnetic remanence and the hysteresis opening, outperforming any previously reported surface adsorbed SMMs, as well as those of bulk samples of $TbPc_2$.[39] Like some metallated phthalocyanines, on some oxides $TbPc_2$ prefers to adopt a standing orientation, with the molecular planes perpendicular to the surface.[65] In this case, the films seem to have an in-plane magnetic anisotropy, while the hysteresis loops show a small butterfly opening at 2K.

The use of graphene as an insulating layer is still unclear. It seems to work for $TbPc_2$ molecules deposited on a layer of graphene on SiC(0001), maintaining the SMM behavior up to 9 K,[66] but not when the substrate underneath graphene is Ni(111).[67]

A different alternative is the encapsulation of the lanthanide ions within an endofullerene.[68] Ever since the discovery of SMM behaviour in the endofullerene $DySc_2N@C80$,[69] new complexes with higher blocking temperatures have been found.[70] The special characteristics of these complexes allow them to maintain remanence when deposited on a layer of graphene on Ir(111),[71] but even directly on metal substrates. For example, when $Dy_2ScN@C80$ is adsorbed on Ag(100), Au(111) and MgO/Ag(100), the electronic interaction decreases dramatically in that order, and the molecular orientation is very different in the three cases, but the measured magnetic hysteresis is roughly the same, the reason being that the charge redistribution at the interface is fully adsorbed by the carbon cage, while the charge state of the endohedral cluster remains intact.[72]

Another lanthanide-containing complex successfully adsorbed in an ordered arrangement on a solid surface is Er(trensal). When deposited directly on Ru(0001) the molecules present different adsorption configurations and an isotropic magnetization. But when deposited on graphene/Ru(0001) or graphene/Ir(111), the molecules are fully oriented with their easy axis of magnetization normal to the surface. However, no magnetic remanence was found in this case even at 3 K[73] (which in this case can be easily explained, since the relaxation time for bulk samples is only of a few milliseconds).[74,75]

Isolated atoms on surfaces

Besides the self-assembly of lanthanide metal-organic complexes, there are additional strategies to form an ordered array of lanthanide atoms on a solid surface, mainly the self-assembly of atoms on a templating support,[76] including the pores of a 2D metal organic network,[77] or the formation of lanthanide-directed metal organic networks (this latter one to be discussed below in a full section). Both cases would allow to reach the ultimate limit in bit size.[78] Actually, it has already been demonstrated that it is feasible to read and write isolated single atoms,[79] being the next frontier how to reproduce such protocols on arrays of lanthanide atoms.

When the atoms are isolated on a substrate and there are no organic ligands, the broken symmetry at the surface is the responsible for the magnetic anisotropy between in-plane and out-of-plane directions, and in some cases a strong uniaxial out-of-plane anisotropy can be generated.[80–83] The effective crystal field can be varied by the choice of substrate and adsorption site. It is worth to mention that in the self-assembly of metal-organic complexes or the design of lanthanide-directed metal-organic networks, the scenario is more complex since it is also necessary an appropriate choice of the ligands to optimize such crystal field.

Substrate-mediated interactions[84] can be used to create atomic superlattices of single atoms on a solid surface, including rare-earth elements.[85,86] However, no magnetic remanence was ever reported on a metallic support following this approach.

Detrimental atom-surface interactions can be minimized by using insulating substrates, which has allowed to measure remanence in single Ho atoms on MgO/Ag(100),[87] or a decoupling layer between the magnetic atom and the metallic substrate, like graphene on Ir(111).[81,88] The highest blocking temperature achieved up to now for isolated atoms, around 40 K, is held by the system of Ho atoms on MgO/Ag(100).[89]

Importantly, by exploiting the Moiré pattern of graphene/Ir(111), an ordered arrangement of Dy atoms could be created, featuring magnetic remanence at very low temperature (2.5 K),[88,90] a finding that sheds light into the design of arrays of isolated, but ordered, lanthanide elements displaying magnetic remanence, by an appropriate choice of lanthanide and crystal field.

Lanthanide-directed metal-organic coordination networks

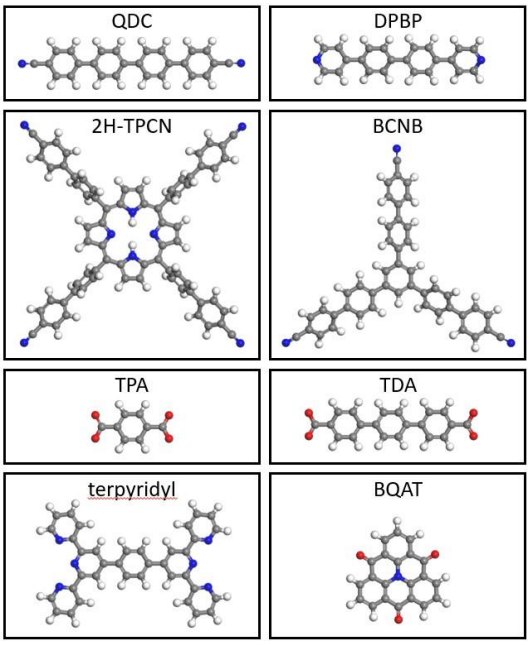

Figure 6. Scheme of the structures of some of the molecules mentioned in the text. QDC = quarterphenyl-4,4''-dicarbonitrile, DPBP = [1,4-bis(4-pyridyl)-biphenyl], 2H-TPCN = tetra[(4-cyanophenyl)phen-4-yl]porphyrin, BCNB = (1,3,5-tris(4'-biphenyl-4''-carbonitrile)benzene, TPA = benzene-1,4-dicarboxylic acid, TDA = p-terphenyl-4,4'-dicarboxylic acid, terpyridyl = 4',4''''-(1,4-phenylene)bis(2,2':6',2''-terpyridine), BQAT = (4H-benzo[9,1]quinolizino[3,4,5,6,7-defg]acridine-4,8,12-trione). Grey, blue, red and white balls represent C, N, O and H atoms, respectively.

Structure

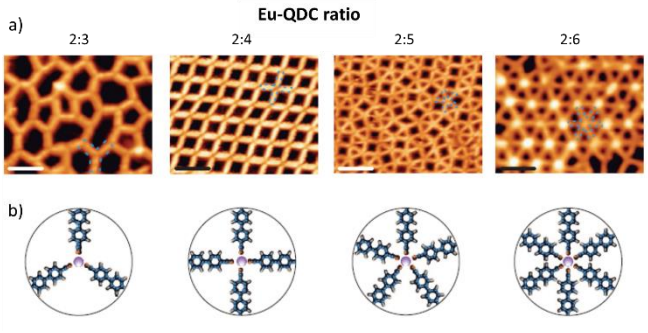

Figure 7. **Eu-directed assembly of MOCNs on Au(111).** a) High-resolution STM images of the distinct coordination networks designed at varying Eu:linker stoichiometries. V_b = −1.2 V, scale bar; 5 nm, T = 300 K. b) Atomistic models highlighting the distinct coordination nodes that stabilize the assemblies: three-fold, four-fold, five-fold and six-fold. Adapted from Ref. [97].

A recent approach to tailor lanthanide atoms in a regular fashion is to design 2D metal-organic coordination networks (MOCNs) on solid. These networks are a reduced-dimensional version of the 3D metal organic frameworks (MOFs), reticular materials made by linking metals and organic units, and that have been the subject of an intense research due to their applicability in many technological and industrial fields.[91]

Although more recent than 3D MOFs, 2D-MOCNs have already been studied for two decades,[92] being the interest in such material recently triggered by the discovery of high conductivity in metal-coordination nanosheets.[93] However, most of the work has been focused on MOCNs containing transition metal elements.[94]

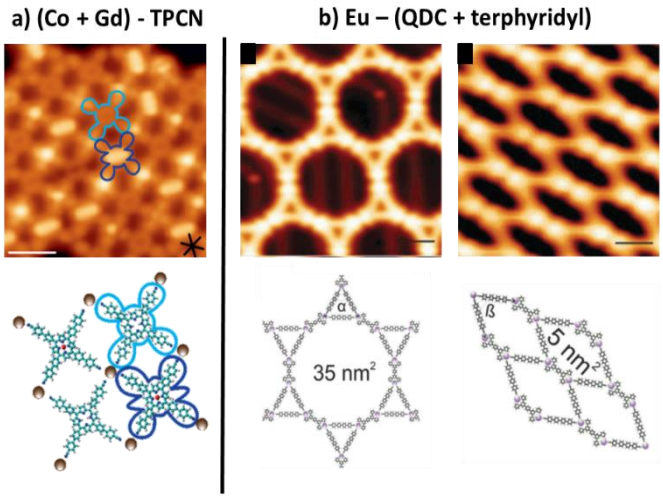

Figure 8. a) A bimetallic porphyrin network comprising Gd and Co centers, obtained by Co deposition on a Gd-TPCN coordination network on Au(111). V_b= -1.2 V, I_t = 100 pA, scale bar: 10 nm, T = 6 K. Reproduced from Ref. [98] with permission © 2015 WILEY-VCH Verlag GmbH & Co. KGaA, Weinheim. b) Two-dimensional porous nanoarchitectures formed upon depositing QDC, terpyridyl and Eu on Au(111). *Left) scale bar: 3nm, T = 6 K; right) scale bar: 2 nm, T = 6 K*. Reproduced from Ref. [99] with permission from the Royal Society of Chemistry. (top) STM images. (bottom) Atomistic models.

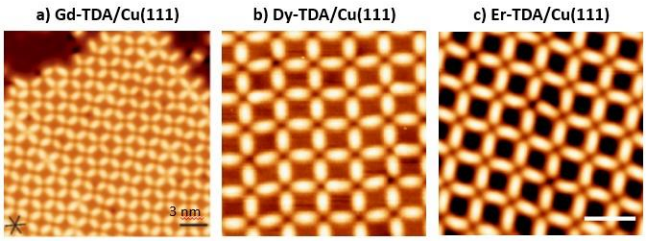

Figure 9. STM images of a) Gd-TDA, b) Dy-TDA and c) Er-TDA square networks on Cu(111). a) V_b = -1 V, It = 300 pA, scale bar: 3 nm, T = 6 K; b) V_b = -1.68 V, I_t =730 pA, 12 nm x 12 nm, T = 300 K; c) V_b = 0.5 V, I_t = 500 pA, scale bar: 3 nm, T = 4 K. Reproduced from (a) Ref. [100] with permission © 2015 WILEY-VCH Verlag GmbH & Co. KGaA, Weinheim; (b,c) Ref. [105] and Ref. [107] with permission under the terms of the Creative Commons CC BY-NC license.

Only recently, the attention was set on lanthanide-based 2D-MOCNs. Figure 6 displays some of the molecular linkers used to that purpose and which will be reviewed in the following.

The on-surface synthesis of 2D MOCNs with lanthanide elements was pioneered in 2013,[95] reporting the formation of different Ce-dicarbonitrile-polyphenyl networks that could tessellate a Ag(111) surface displaying five-vertex Archimedean motifs.[95] Similar results were obtained with (NC-(Ph)3-CN) or (NC-(Ph)4-CN), or when Ce was replaced by Gd.[96] A later detailed study, using Eu as the lanthanide atom (with an expected +2 oxidation state), showed that the type of arrangement was strongly dependent on the exact stoichiometry between the lanthanide atom and the molecular linker, going from disordered to square ordered arrangements, and from quasicrystalline structures to even six-fold coordinated structures on Au(111) (Figure 7).[97,98]

Bimetallic networks have also been reported. After depositing Gd and a free-base porphyrin derivative

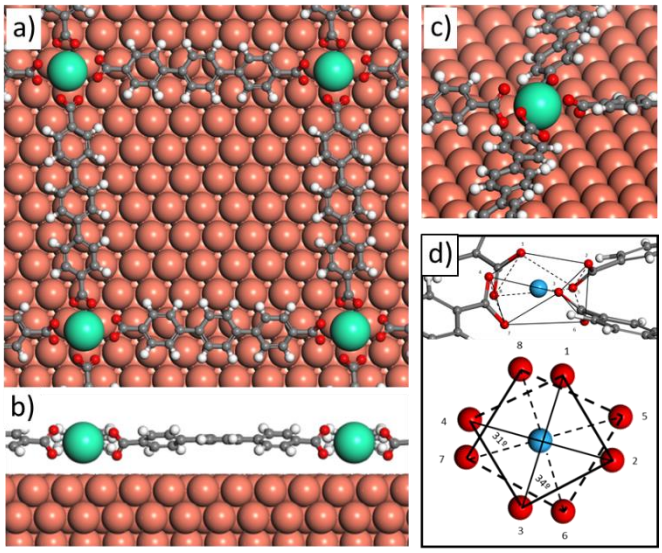

Figure 10. a,b) Top and side view of the calculated DFT structure of the Dy-TDA coordination network on Cu(111). c,d) Details of the coordination geometry, showing the distorted antiprism formed by the O atoms. Adapted from Ref. [105] with permission under the terms of the Creative Commons CC BY-NC license.

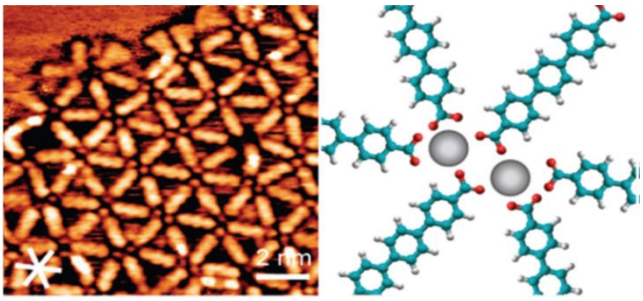

Figure 11. STM image of a dinuclear hexagonal Dy-TDA network on Cu(111) created by annealing to 450 K the square network shown in Figure 9b. *V_b = -1,2 V, I_t = 320 pA.* Reproduced from Ref. [101] with permission from the Royal Society of Chemistry.

functionalized with meso-cyanobiphenylene substituents (TPCN) on Ag(111), a square-planar motif is formed that reflects the fourfold coordination of the -CN ligands to the rare-earth centers; that is, each Gd atom is coordinated to four –CN groups of four different porphyrins. When depositing Co on this network, the Co atoms tend to metallate the porphyrin cores, without disturbing the Gd-TPCN lattice, ultimately leading to a d-f hybrid array with the topology of an alternating bimetallic square grid (see Figure 8a).[98]

Alternatively, bimolecular metal-organic networks could also be grown on Au(111) by combining Eu with two different molecular ligands (QDC and terpyridyl) equipped, respectively, with carbonitrile and terpyridyl terminals. For the appropriate stoichiometry (QDC:terpyridyl = 1.8) two different periodic structures, hexagonal and rhombohedral, are obtained (see Figure 8c-f). In both cases the Eu atom is five-fold coordinated, with 3 N atoms from one terpyridyl molecule, and 2 N atoms from two different QDC ligands, the only difference being the surface molecular density.[99]

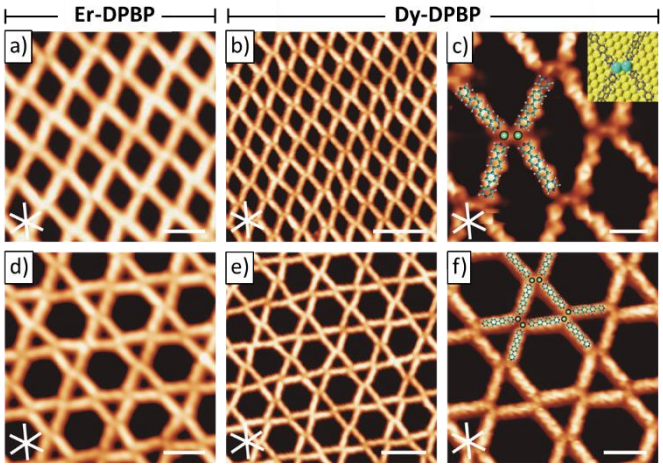

Figure 12. STM images of the two different dinuclear networks a,d) Er-DPBP and b,c,e,f) Dy-DPBP on Au(111). (a-c) Rhombic networks, (d-f) Kagome networks. *a) V_b = 0.5 V, I_t = 100 pA, scale bar: 3 nm; b) V_b = -1.V, I_t = 50 pA; scale bar: 4 nm; c) V_b = 0.005 V, I_t = 50 pA, scale bar: 1nm; d) V_b = 0.5 V, I_t = 200 pA, scale bar: 3nm; e) V_b = -0.3 V, I_t = 200 pA, scale bar: 4 nm; f) V_b = -0.1 V, I_t = 1500 pA, scale bar: 2 nm. T = 4.3 K.* Reproduced from Ref. [106] with permission under the terms of the Creative Commons CC BY-NC license.

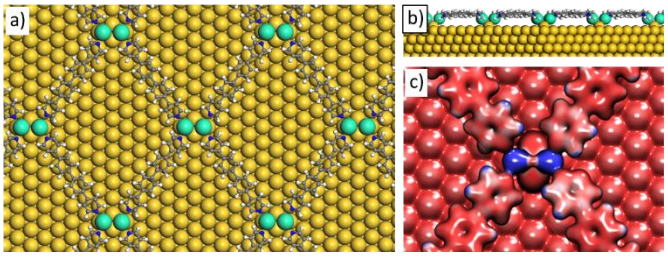

Figure 13. a,b) DFT calculated structure of the rhombohedral Dy-DPBP network on Au(111). (a)Top and (b) side views. c) Electronic isosurface showing the formation of a bond between the Dy atoms. Adapted from Ref. [106] with permission under the terms of the Creative Commons CC BY-NC license.

Subsequent work demonstrated the possibility of forming thermally robust regular networks with Gd atoms on Cu(111) when the nitrile groups were replaced by carboxylate moieties.[100] The scanning tunnelling microscopy (STM) images showed an almost square lattice with a unit cell of 19.5 Å (see Figures 9a and 10), where each lanthanide atom was four-fold coordinated to eight O atoms (from 4 different molecules). The same arrangement was found when Gd was replaced by Dy (Figure 9b).[101] This work also showed how the size of the cavity could be tuned by an appropriate choice of the organic linker (TPA instead of TDA). A similar Ho-TPA network was later reported on Ag(100).[102] Importantly, according to the STM images and DFT calculations (see Figure 10), each lanthanide atom was linked to 4 TDA molecules (which implies lanthanide coordination with 8 O atoms). The main difference with the five-fold coordination found with the dicarbonitrile-polyphenyl species is that now steric hindrance between the carboxylate terminals forbids coordination with more than four organic ligands.

In addition to these square lattices, hexagonal structures were found when annealing the Dy-TDA network to 450 K, most probably due to the change in stoichiometry, from Dy:TDA = 1:2 (square) to Dy:TDA = 2:3 (hexagonal). A careful look, however, revealed that the new arrangement is based on dinuclear Dy nodes in which the Dy centres are distanced by 5.8 Å (see Figure 11). The atomistic model reveals a unique coordination motif, whereby each Dy centre is engaged in six Dy···O coordination bonds, and in which four molecules are connected to one single dysprosium and the two additional linkers are sharing the two Dy atoms.

Dinuclear nodes can be found for other stoichiometries as well. Figure 12 shows two different networks, rhombohedral and Kagome-like, formed by DPBP and either Dy or Er (in both cases the structures are very similar) on Au(111). A closer look reveals that the nodes are composed of two lanthanide atoms, which stoichiometry is Ln:DPBP = 1:1.

Similar (and other) lattices where the nodes contained 2, 3 or 4 lanthanide atoms were found on Au(111) and Au(100) when using Ce as the lanthanide atom.[103] However, in that work the authors claimed that the formation of these Ce clusters was possible due to the participation of Au adatoms acting as bridges between the lanthanide atoms. However, for the Dy or

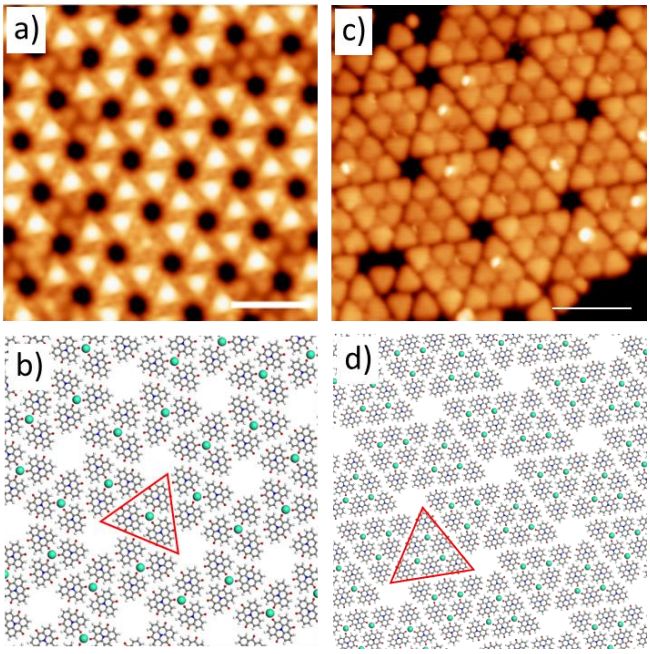

Figure 14. The different coordination networks formed by Dy and BQAT on Au(111) upon variation of the Dy:BQAT stoichiometry for a,b) BQAT:Dy=3:1 and c,d) BQAT:Dy=6:3. (a,c) STM images and (b,d) atomistic models. a) *V_b = 0.5 V, I_t = 50 pA, scale bar: 4 nm, T = 4.3 K; c) V_b = 0.05 V, I_t = 80 pA, scale bar: 3 nm. T = 4.3 K.* Adapted from Ref. [104]

Er-directed cases, though calculations reveal that some Au atoms are slightly pulled out from the surface, (Figure 13b), there is no experimental nor theoretical evidence of any real Au adatom. The main difference among these systems seems to be the Ln-Ln distance. While for the Ce-DPBD case it was around 4.5 – 5.0 Å, in the Dy or Er cases it is around 3.0 Å, which is much closer to the distance between Ln atoms in either Dy or Er bulk. Actually, DFT calculations show that the atoms are so close together that there is an electronic bond between them (Figure 13c).

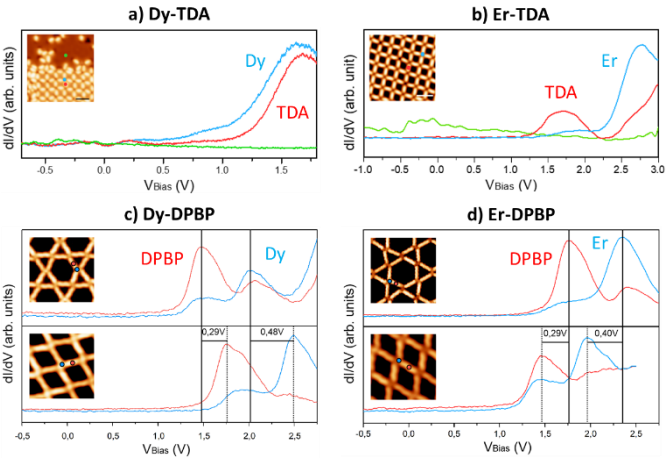

Figure 15. dI/dV spectra taken on the metal center and the molecular linker for the coordination networks of a) Dy-TDA and b) Er-TDA on Au(111); c) Dy-DPBP and d) Er-DPBP on Cu(111). *STS spectra measured with an open feedback loop and a lock-in modulation of a) 10 mV; b,c,d) 20 mV*. Adapted from (a) Ref. [105], (b) Ref. [107], and (c,d) Ref. [106], with permission under the

Recently, the number of functional groups used to create lanthanide-organic coordination networks has been expanded to include the ketone group.[104] When BQAT molecules are deposited on Au(111), a Dy-BQAT coordinated network is formed (Figure 14). In this case, due to steric hindrance, the coordination number is only 3, being each Dy atom coordinated with 3 BQAT molecules through the –C=O groups. This case is a clear example of hierarchical growth. For a BQAT:Dy=3:1 stoichiometric ratio, nuclei formed by 1 Dy atom and 3 BQAT molecules (tectons) self-assemble through hydrogen bonds to create an hexagonal porous lattice. When the stoichiometry increases to BQAT:Dy=6:3, the nuclei are formed by 6 molecules coordinated with 3 Dy atoms, though still featuring a long-range hexagonal porous lattice of higher intermodal distance.

Electronic properties

Although there has been a gradual increase in reports regarding the fabrication of lanthanide-directed metal-organic coordination networks, studies concerning their electronic and magnetic properties remain very scarce. In the following, we aim to showcase the majority of research conducted in this field thus far.

For Gd on Cu(111), Dy and Er, either on Cu(111) or Au(111), when measured by XPS[100,101] or XAS[105–107] (see below), the oxidation state seems to be +3 in all cases (although the DFT results invariable indicate a slightly smaller positive charge).[100,102,105–107] The Er-TDA/Cu(111) result is in contrast with the behavior of isolated Er atoms on the same surface,

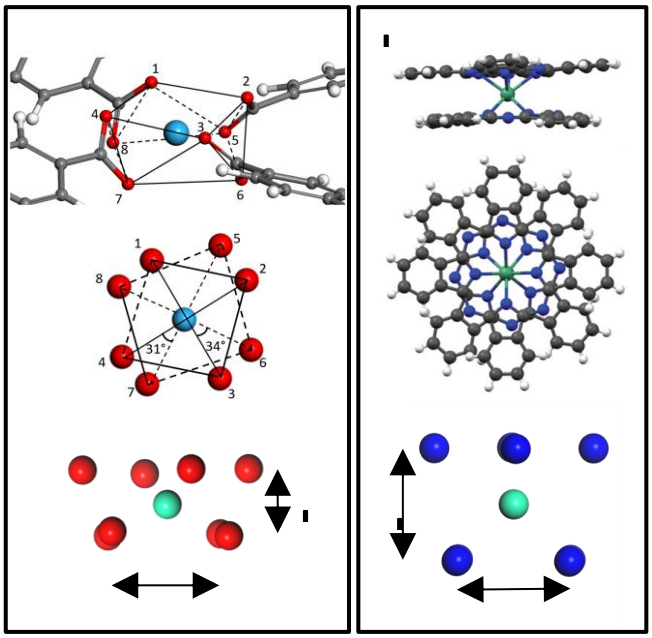

Figure 16. Structure of Dy-based molecular magnets. (a) Dy-TDA crystal field symmetry, where grey, white, red, and blue balls represent C, N, O and Dy, respectively. Reproduced from Ref. [101] with permission under the terms of the Creative Commons CC BY-NC license. (b) DyPc2, where dark grey, blue, light grey and turquoise balls represent C, N, H and Dy, respectively. Reproduced from Ref. [63] with permission under the terms of the Creative Commons CC BY license.

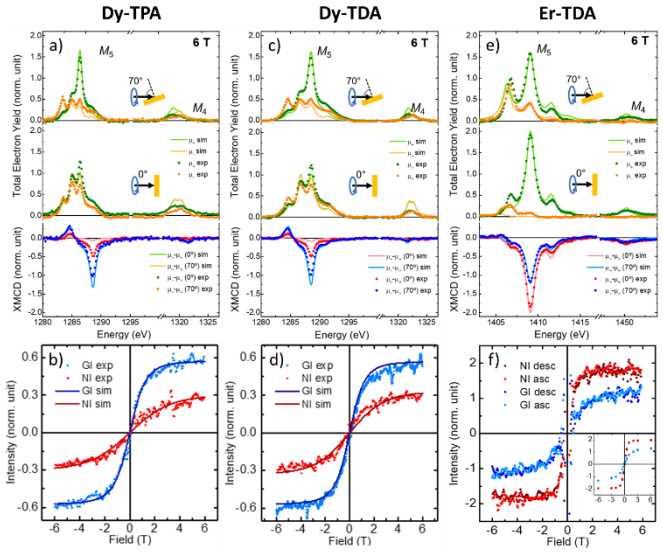

Figure 17. Magnetic properties of Dy-TDA and Er-TDA based mononuclear metal-organic networks. a,c,e) XAS spectra acquired with negative (μ-, orange) and positive (μ+, green) circularly polarized light and XMCD (μ-μ+) taken at Dy $M_{4,5}$-edges at normal (0°, red) and grazing (70°, blue) incidences for: (a) Dy-TPA, (c) Dy-TDA, and (e) Er-TDA networks. (B = 6 T, T = 6 K). The experimental data is presented by dots and multiplet calculations are presented as brighter lines. (B = 6 T, T = 6 K) b,d,f) Magnetization curves for (b) Dy-TPA, (d) Dy-TDA, and (f) Er-TDA. Adapted from Ref. [101] and Ref. [103] with permission under the terms of the Creative Commons CC BY-NC license.

where XAS measurements indicate a +2 oxidation state.[80] On the contrary, the low value of the charge transfer calculated by DFT for Ho-TPA/Ag(100) [102] suggests a +2 oxidation state, which is the same than isolated atoms present on Ag(100).[80]

Figure 15 shows dI/dV spectra for the few reported systems so far.[105,106] Herein, important findings deserve some comments. First, the TDA:lanthanide mononuclear architecture displays no change in the energy level alignment of the molecular species upon exchange of Dy by Er centers on Cu(111). On the contrary, for DPBP:lanthanide dinuclear architectures on Au(111), there is a shift in the main peaks associated with the molecular resonances when moving from Dy to Er (although they are very similar for each dinuclear lattices). A similar shift (although smaller in magnitude) is observed between the two dinuclear lattices for the peaks assigned to the lanthanide centers. Importantly, the distinct energy positions of the resonances between TDA:lanthanide and the two phases of DBPB:lanthanide architectures can be easily explained by the different coordination.

These results show that it is feasible to tune the energy level alignment of a lanthanide-based metal-organic architecture, while maintaining the same structure, by simply substituting the lanthanide element, which is of crucial relevance for the potential implementation of such networks on devices.

Magnetic properties

As mentioned above, the linkage of lanthanides and organic molecules in metal-organic frameworks (MOFs) allows the engineering of ordered architectures with tailorable properties.[108–110] The combination of the chemical tunability, long range ordering and porosity makes this kind of system an ideal playground for the development of lanthanide-based magnets. The versatility of the molecular linkers available has led to the report of 3D and surface-confined 2D lanthanide-directed MOFs in the last years. [111]

	normal	grazing	ΔM
Dy-TPA/Cu(111)	2.2	5.1	-2.9
Dy-TDA/Cu(111)	2.2	4.7	-2.4
Er-TDA/Cu(111)	9.7	5.4	4.8
Dy-DPBP/Au(111)	3.9	8.4	-4.6
Er-DPBP/Au(111)	6.7	5.8	0.9

Table 2. Experimental magnetic moments (in units of μ_B) measured by XMCD, in both normal and grazing incidence, for the lanthanide networks reported. The magnetic moments have been obtained by using the formula $\mu = 2S + L$, where S and L are calculated from the XMCD results following the sum rules. Caution must be taken, however, because the calculated S includes a Tz term in principle hard to estimate.

As we have discussed above, the first studies on lanthanide molecular magnets on surfaces were focused mainly on double-deckers,[36–39,63,112] and only recently the magnetic properties of 2D lanthanide metal-organic networks on surfaces have been reported by us.[105–107]

In parallel, a study of lanthanide-directed 1D organometallic wire was reported.[113,114] The deposition of Eu and cyclooctatetraene (COT) on graphene/Ir(111) gives rise to molecular wires, in which COT linkers are adsorbed with their main plane perpendicular to the surface, establishing bonds with Eu atoms located in between two adjacent COT species.[114] The magnetic characterization seem to indicate a ferromagnetic coupling of the Eu atoms, with the direction of easy axis magnetization in the surface plane.[113]

The seminal study of 2D lanthanide-directed coordinative architectures reports the magnetic properties of 2D networks based on carboxylic molecular linkers (TDA, TPA) coordinated with Dy atoms on a Cu(111) surface.[105] Such coordination gives rise to almost square mononuclear networks where each Dy atom is coordinated to eight nitrogen atoms from four adjacent molecules (Figure 10). The effective coordination gives rise to a distorted square antiprism crystal field (see Figure 16a) that has a symmetry similar to the $DyPc_2$ species described previously (Figure 16b). However, for Dy-TDA and Dy-TPA architectures the orientation of the magnetic anisotropy is close to the surface plane (see Figure 17a-d), with the easy axis tilted around ~70° away from the surface normal,[105] in opposition to the out-of-plane anisotropy observed for $DyPc_2$.[38,63,115] To rationalize such findings it is helpful to revise literature. A system with related symmetry is the $[Na\{Dy(DOTA)(H_2O)\}]\cdot 4H_2O$ salt (Dy-DOTA), which presents a Dy atom in a sandwich-type coordination featuring a square antiprism, the only difference being the capping with a water molecule, which turns out to be crucial.[116,117] In this case the magnetization easy axis is almost perpendicular to the symmetry axis, similarly to the Dy-TDA and Dy-TPA networks. However, it can be drastically changed if the water molecule is removed or rotated.[116,117] Moreover, when

comparing Dy-TDA and Dy-TPA, the orientation and intensity are slightly different even if the molecular coordination is very similar.[105] These differences are attributed to minor changes in the crystal field environment. Such results indicate that the orientation of the magnetic anisotropy on molecular magnets is very sensitive to subtle changes in the crystal field environment.

When considering the same TDA molecules coordinated with another lanthanide ion, erbium, the structure of the Er-TDA network is analogous to the Dy-TDA architecture, featuring an almost square lattice (Figure 11c),[105,107]. However, there is a significant difference in the inherent magnetic properties. While the Dy-TDA assembly features a close to in-plane anisotropy as described before, for the Er-TDA network the orientation of the magnetic easy-axis is perpendicular to the surface plane (see Figures 17e,f), following the symmetry axis of the crystal field.[107] The Dy atoms in the Dy-TDA have high magnetic moments and anisotropies (Table 2),[105] but these values are even higher for Er-TDA, and the quantum number J_z has the maximum value possible for a Er^{3+} ion, 15/2.[107] These differences on the magnetic anisotropies for Dy and Er networks can also be observed in the magnetization curves measured at normal and grazing incidents (NI and GI, respectively). While for Dy-TDA the magnetization curve at GI is closer to saturation than at NI (see Figure 17d), for Er-TDA the curve measured at NI seems to be already saturated in contrast to GI where a full saturation was not yet achieved at 6 T (Figure 17f).

For both Dy and Er ions of TDA network the oxidation state is +3, meaning an oblate charge density for Dy and a prolate for Er (see Figure 4a). According to the model from Figure 4b, in principle the apparently sandwich-type coordination of the TDA networks should be favourable to increase the anisotropy of oblate ions, like Dy^{3+}, but detrimental for prolate ions, like Er^{3+}. However, the experimental results show that the effective crystal field of the TDA networks is more favourable for Er^{3+}, that presents a higher anisotropy than the Dy^{3+}.[107] The reason behind this apparent contradiction is that the antiprism formed by the 8 O atoms is strongly compressed in the vertical direction, in such a way that the coordination environment is far from being the regular sandwich-type. DFT calculations for the gas phase structure show that, while the side of the squares is d = 3.19 Å, the height is only h = 1.95 Å. In addition, the interaction with the surface makes the molecules to flatten against the surface, reducing the height even more to h = 1.75 Å (d = 3.40 Å) (see Figure 16b). In contrast, in the antiprism formed by the 8 N atoms in $DyPc_2$ (see Figure 16a) h and d are almost the same (d = 3.01 Å, h = 2.98 Å). Considering that the ionic radii of Ln^{3+} ions is around 1.1 Å, the final result is that the lanthanide atom is closer to be equatorially, rather than axially, coordinated, favouring the axial anisotropy of the prolate Er^{3+} ion, in accordance with the proposed oblate-prolate model. Once again, these results point out the importance of the exact geometry of the surroundings and its effect in the generated crystal field.

An additional important aspect in molecular magnetism involving lanthanide-directed metal-organic networks is the design of multinuclear centers of coordination. The coupling between metallic centers in such nodes could lead to an

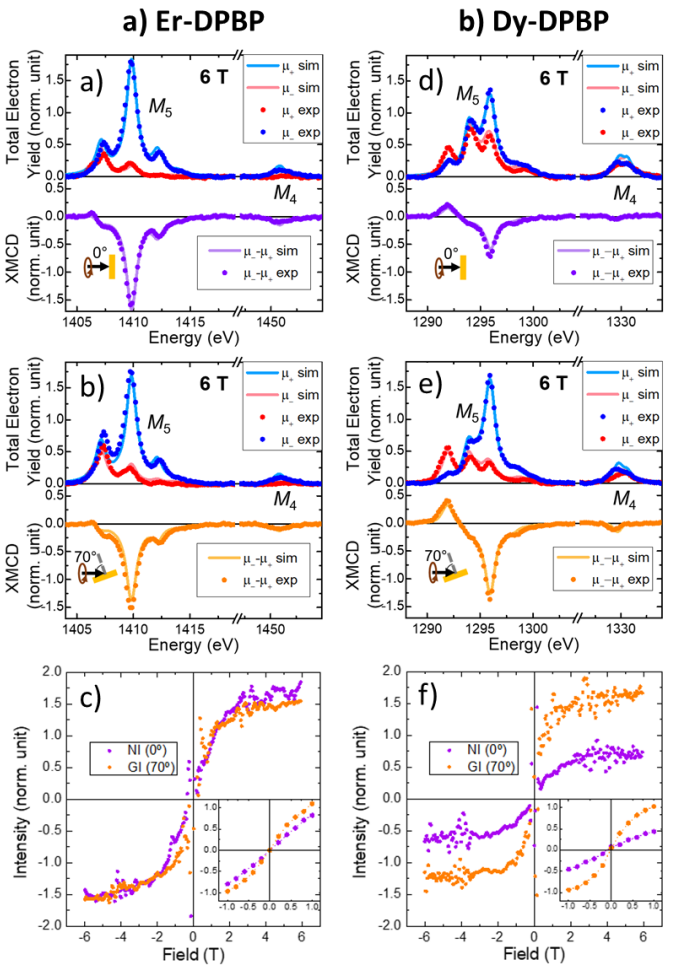

Figure 18. Magnetic properties of Er-DPBP and Dy-DPBP based dinuclear metal-organic networks. a,b,d,e) XAS spectra acquired with negative (μ_-, red) and positive (μ_+, blue) circularly polarized light and XMCD (μ_--μ_+) taken at Er/Dy $M_{4,5}$-edges at normal (0°, purple and grazing (70°, orange) incidences for: (a,b) Er-DPBP-TPA and (d,e) Dy-DPBP networks. (B = 6 T, T = 1.6 K) c,f) Magnetization curves for (c) Er-DPBP, and (f) Dy-DPBP. Reproduced from Ref. [106] with permission under the terms of the Creative Commons CC BY-NC license.

improvement of the magnetic properties, including larger energy splitting levels, higher energy barriers and longer relaxation times.[6] Here, it is worth to mention that the actual coercive field record in lanthanide complexes is held by a mixed-valence Dy-Cp compound, containing two Dy atoms with a very high exchange coupling.[33]

One example of dinuclear networks is shown in Figure 12, in which Dy and Er atoms, respectively, are coordinated with DPBP molecular linkers on a Au(111) surface.[106] Depending on the coverage, two distinct metallosupramolecular architectures are observed: rhombic or Kagome. In both cases, similarly to the TDA systems, the networks preserve the same structure when the metal is exchanged between Er and Dy, and the oxidation state is +3 for both metals.[106] However, like in the Dy- or Er-TDA cases, when the magnetic properties of the rhombic architecture were investigated, significant differences were found between the Dy- and Er-directed lattices. For the Er-DPBP system, although the XMCD intensities and magnetic moments

are very similar for both grazing and normal incidences (Figures 18a,b), careful measurements of the magnetization curves (see the inset in Figure 18c), show that the slope of the M vs. H curve is greater for grazing incidence than for normal incidence, pointing to an easy axis closer to in-plane than out-of-plane. Actually, multiplet calculations based on the MultiX code, which reproduce fairly well the experimental results, indicate that the easy axis is tilted 50° away from the surface normal. In the case of the Dy-DPBP architecture the easy axis of magnetization is close to the surface plane, around 80° with respect to the surface normal, and the XMCD intensity and magnetic moments are higher at grazing incidence than at normal (see Figures 18d,e). According to the multiplet calculations, J_z is 15/2 for both Er and Dy metallic centers, indicating purely axial systems.

Table 2 shows the magnetic moments, calculated using the sum rules,[118,119] for the studied lanthanide-directed metallosupramolecular networks reported so far (the mononuclear Dy-TDA and Er-TDA, and the dinuclear Dy-DPBB and Er-DPBB), both in normal and grazing incidences. The results show that, for these particular ligands, the magnetic moments measured for Dy at grazing incidence are always larger than at normal incidence, while the reverse is true for Er.

Growth on decoupling substrates

As we have seen metal-organic coordination directed by lanthanides is a feasible strategy to design long-range order arrangements of magnetic atoms on a solid surface. In addition, the magnetic anisotropy can be tuned by an appropriate choice of lanthanide atom and/or organic ligand. However, up to know, no magnetic remanence has been reported on metallic supports for such metallosupramolecular architectures. Inspired by previous results on SMMs on surfaces, the following logical step would be to grow these lattices on non-metallic substrates.

To this end, we have tried to grow a Dy-BCNB coordination network on graphene/Ir(111). Figure 19 shows some STM images of this network. Although the general appearance resembles a hexagonal lattice with six-fold coordinated nodes, careful measurements of the experimental results and DFT calculations of the different coordination configurations reveal that actually there are two types of nodes: mononuclear, based on a five-fold coordination number, and dinuclear, relying on a three-fold Dy-BCNB coordination.[120] These findings reveal the feasibility of engineering lanthanide-directed metal-organic networks on graphene, paving avenues to explore the promising magnetic properties of rare-earth elements in low dimensional systems.

Conclusions

The study of the magnetic properties of lanthanide-directed metallosupramolecular architectures on surfaces, and their possible use as SMMS, is still at its infancy. Here, we have reported the very preliminary findings of this fascinating topic of research.

Coordination chemistry on metal surfaces has been revealed as a powerful strategy to engineer periodic or quasiperiodic architectures, mostly based on mononuclear nodes, but also opening opportunities for multinuclear centers of coordination and bimolecular architectures. The next frontier would be to export such increasing chemical knowledge to decoupling supports like graphene or hexagonal boron nitride, or oxides like MgO, to explore the influence on the lanthanide physicochemical properties of less perturbative substrates.

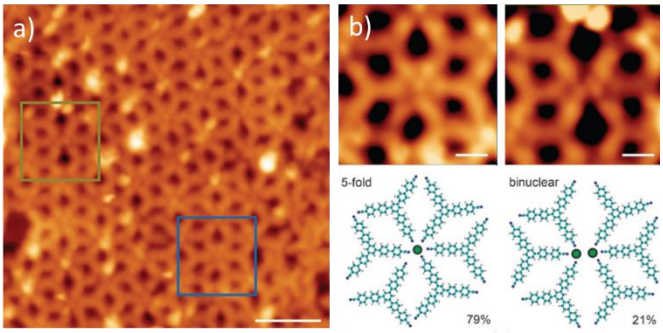

Figure 19. a) Overview STM image of the Dy-BCNB network on graphene/Ir(111). b) Zoom-in STM images and atomistic models of the two different types of nodes. *V_t = 0.5 V, I_t = 10 pA. a) scale bar: 4 nm; b) scale bar: 1 nm.* Reproduced from Ref. [120] with permission under the terms of the Creative Commons CC BY-NC license.

Remarkably, in some of the reported cases the exchange of lanthanide atom preserves the chemical structure, while allowing to modify the electronic and magnetic properties. It is feasible to tune the energy level alignment between the metal-organic overlayer and the underlying substrate. In addition, it is possible to tailor the magnetic anisotropy, not only in magnitude, but in direction, changing from in-plane to out-of-plane anisotropy.

Thanks to the versatility of coordination chemistry, the chemical combinations by selecting appropriate lanthanide elements, linkers and substrates seem endless, envisioning a promising pathway for the emerging field of magnetic lanthanide-directed metallosupramolecular architectures on surfaces, with great potential impact both in information storage and quantum information.[121,122]

Author Contributions

All authors contributed equally to this work.

Conflicts of interest

There are no conflicts to declare.

Acknowledgements

This project has received funding from the European Research Council (ERC, grant 766555) and Marie Sklodowska-Curie Actions (MSCA, project 894924) under the European Union's Horizon 2020 research and innovation program, and from Spanish MINECO (PID2019-108532GB-I00). IMDEA Nanociencia is appreciative of

support from the "Severo Ochoa" Programme for Centers of Excellence in R&D (MINECO, grant SEV-2016-0686).

1. Sessoli, R., Gatteschi, D., Caneschi, A. & Novak, M. A. Magnetic bistability in a metal-ion cluster. *Nature* **365**, 141–143 (1993).
2. Ishikawa, N., Sugita, M., Ishikawa, T., Koshihara, S. Y. & Kaizu, Y. Lanthanide double-decker complexes functioning as magnets at the single-molecular level. *J. Am. Chem. Soc.* **125**, 8694–8695 (2003).
3. Leuenberger, M. N. & Loss, D. Quantum computing in molecular magnets. *Nature* **410**, 789–793 (2001).
4. Zabala-Lekuona, A., Seco, J. M. & Colacio, E. Single-Molecule Magnets: From Mn12-ac to dysprosium metallocenes, a travel in time. *Coord. Chem. Rev.* **441**, 213984 (2021).
5. Marin, R., Brunet, G. & Murugesu, M. Shining New Light on Multifunctional Lanthanide Single-Molecule Magnets. *Angew. Chemie Int. Ed.* **60**, 1728–1746 (2021).
6. Chen, Y.-C. & Tong, M.-L. Single-molecule magnets beyond a single lanthanide ion: the art of coupling. *Chem. Sci.* (2022) doi:10.1039/D2SC01532C.
7. Feltham, H. L. C. & Brooker, S. Review of purely 4f and mixed-metal nd-4f single-molecule magnets containing only one lanthanide ion. *Coord. Chem. Rev.* **276**, 1–33 (2014).
8. Dreiser, J. Molecular lanthanide single-ion magnets: From bulk to submonolayers. *Journal of Physics Condensed Matter* vol. 27 (2015).
9. *Rare Earth Coordination Chemistry: Fundamentals and Applications*. (John Wiley and Sons, 2010). doi:10.1002/9780470824870.
10. *The Rare Earth Elements: Fundamentals and Applications*. (John Wiley & Sons Ltd, 2012).
11. Benelli, C. & Gatteschi, D. (Dante). Introduction to molecular magnetism : from transition metals to lanthanides.
12. Molecular Nanomagnets and Related Phenomena. **164**, (2015).
13. Zhu, Z., Guo, M., Li, X. L. & Tang, J. Molecular magnetism of lanthanide: Advances and perspectives. *Coordination Chemistry Reviews* vol. 378 350–364 (2019).
14. Chibotaru, L. F. *et al.* Structure, magnetism, and theoretical study of a mixed-valence Co II3CoIII4 heptanuclear wheel: Lack of SMM behavior despite negative magnetic anisotropy. *J. Am. Chem. Soc.* **130**, 12445–12455 (2008).
15. C Feltham, H. L. *et al.* A Non-sandwiched Macrocyclic Monolanthanide Single-Molecule Magnet: The Key Role of Axiality. *Chem. – A Eur. J.* **17**, 4362–4365 (2011).
16. Neese, F. & Pantazis, D. A. What is not required to make a single molecule magnet. *Faraday Discuss.* **148**, 229–238 (2010).
17. Craig, G. A. & Murrie, M. 3d single-ion magnets. *Chem. Soc. Rev.* **44**, 2135–2147 (2015).
18. Frost, J. M., Harriman, K. L. M. & Murugesu, M. The rise of 3-d single-ion magnets in molecular magnetism: towards materials from molecules? *Chem. Sci.* **7**, 2470–2491 (2016).
19. Guo, F.-S. *et al.* A Dysprosium Metallocene Single-Molecule Magnet Functioning at the Axial Limit. *Angew. Chemie Int. Ed.* **56**, 11445–11449 (2017).
20. Goodwin, C. A. P., Ortu, F., Reta, D., Chilton, N. F. & Mills, D. P. Molecular magnetic hysteresis at 60 kelvin in dysprosocenium. *Nature* **548**, 439–442 (2017).
21. Guo, F. S. *et al.* Magnetic hysteresis up to 80 kelvin in a dysprosium metallocene single-molecule magnet. *Science (80-.).* **362**, 1400–1403 (2018).
22. Nicholas, H. M. & Mills, D. P. Lanthanides: Divalent Organometallic Chemistry. in *Encyclopedia of Inorganic and Bioinorganic Chemistry* 1–10 (John Wiley & Sons, Ltd, 2017). doi:10.1002/9781119951438.EIBC2453.
23. Farnaby, J. H., Chowdhury, T., Horsewill, S. J., Wilson, B. & Jaroschik, F. Lanthanides and actinides: Annual survey of their organometallic chemistry covering the year 2019. *Coord. Chem. Rev.* **437**, 213830 (2021).
24. Rinehart, J. D. & Long, J. R. Exploiting single-ion anisotropy in the design of f-element single-molecule magnets. *Chem. Sci.* **2**, 2078–2085 (2011).
25. Zhang, P. *et al.* Equatorially coordinated lanthanide single ion magnets. *J. Am. Chem. Soc.* **136**, 4484–4487 (2014).
26. Ishikawa, N. *et al.* Determination of ligand-field parameters and f-electronic structures of double-decker bis(phthalocyaninato)lanthanide complexes. *Inorg. Chem.* **42**, 2440–2446 (2003).
27. Xiong, J. *et al.* Hydroxide-bridged five-coordinate Dy III single-molecule magnet exhibiting the record thermal relaxation barrier of magnetization among lanthanide-only dimers. *Chem. Sci.* **8**, 1288–1294 (2017).
28. Westerström, R. *et al.* An endohedral single-molecule magnet with long relaxation times: DySc 2N@C 80. *J. Am. Chem. Soc.* **134**, 9840–9843 (2012).
29. Jeletic, M. *et al.* An Organometallic Sandwich Lanthanide Single-Ion Magnet with an Unusual Multiple Relaxation Mechanism. *J. Am. Chem. Soc.* **133**, 19286–19289 (2011).
30. Ding, Y.-S., Chilton, N. F., Winpenny, R. E. P. & Zheng, Y.-Z. On Approaching the Limit of Molecular Magnetic Anisotropy: A Near-Perfect Pentagonal Bipyramidal Dysprosium(III) Single-Molecule Magnet. *Angew. Chemie Int. Ed.* **55**, 16071–16074 (2016).
31. Liu, J. *et al.* A Stable Pentagonal Bipyramidal Dy(III) Single-Ion Magnet with a Record Magnetization Reversal Barrier over 1000 K. *J. Am. Chem. Soc.* **138**, 5441–5450 (2016).
32. Woodruff, D. N., Winpenny, R. E. P. & Layfield, R. A. Lanthanide single-molecule magnets. *Chem. Rev.* **113**, 5110–5148 (2013).
33. Gould, C. A. *et al.* Ultrahard magnetism from mixed-valence dilanthanide complexes with metal-metal bonding. *Science (80-.).* **375**, 198–202 (2022).
34. Gabarró-Riera, G., Aromí, G. & Sañudo, E. C. Magnetic molecules on surfaces: SMMs and beyond. *Coord. Chem. Rev.* **475**, 214858 (2023).
35. Moreno Pineda, E., Komeda, T., Katoh, K., Yamashita, M. & Ruben, M. Surface confinement of TbPc2-SMMs:

structural, electronic and magnetic properties. *Dalt. Trans.* **45**, 18417–18433 (2016).
36. Stepanow, S. *et al.* Spin and orbital magnetic moment anisotropies of monodispersed bis(Phthalocyaninato)terbium on a copper surface. *J. Am. Chem. Soc.* **132**, 11900–11901 (2010).
37. Margheriti, L. *et al.* Spin and orbital magnetic moment anisotropies of monodispersed bis(Phthalocyaninato)terbium on a copper surface. *Adv. Mater.* **22**, 5488–5493 (2010).
38. Klar, D. *et al.* Hysteretic behaviour in a vacuum deposited submonolayer of single ion magnets. *Dalt. Trans.* **43**, 10686–10689 (2014).
39. Wäckerlin, C. *et al.* Giant Hysteresis of Single-Molecule Magnets Adsorbed on a Nonmagnetic Insulator. *Adv. Mater.* **28**, 5195–5199 (2016).
40. Ara, F. *et al.* A scanning tunneling microscopy study of the electronic and spin states of bis(phthalocyaninato)terbium(III) (TbPc2) molecules on Ag(111). *Dalt. Trans.* **45**, 16644–16652 (2016).
41. Mannini, M. *et al.* XAS and XMCD Investigation of Mn12 Monolayers on Gold. *Chem. – A Eur. J.* **14**, 7530–7535 (2008).
42. Cavallini, M., Facchini, M., Albonetti, C. & Biscarini, F. Single molecule magnets: from thin films to nano-patterns. *Phys. Chem. Chem. Phys.* **10**, 784–793 (2008).
43. Gatteschi, D., Cornia, A., Mannini, M. & Sessoli, R. Organizing and addressing magnetic molecules. *Inorg. Chem.* **48**, 3408–3419 (2009).
44. Domingo, N., Bellido, E. & Ruiz-Molina, D. Advances on structuring, integration and magnetic characterization of molecular nanomagnets on surfaces and devices. *Chem. Soc. Rev.* **41**, 258–302 (2011).
45. Scudiero, L., Barlow, D. E. & Hipps, K. W. Physical Properties and Metal Ion Specific Scanning Tunneling Microscopy Images of Metal(II) Tetraphenylporphyrins Deposited from Vapor onto Gold (111). *J. Phys. Chem. B* **104**, 11899–11905 (2000).
46. Auwärter, W., Écija, D., Klappenberger, F. & Barth, J. V. Porphyrins at interfaces. *Nat. Chem.* **7**, 105–120 (2015).
47. Zhang, Y. F. *et al.* A Low-Temperature Scanning Tunneling Microscope Investigation of a Nonplanar Dysprosium−Phthalocyanine Adsorption on Au(111). *J. Phys. Chem. C* **113**, 14407–14410 (2009).
48. Weber-Bargioni, A. *et al.* Interaction of Cerium Atoms with Surface-Anchored Porphyrin Molecules. *J. Phys. Chem. C* **112**, 3453–3455 (2008).
49. Cirera, B. *et al.* Long-Range Orientational Self-Assembly, Spatially Controlled Deprotonation, and Off-Centered Metalation of an Expanded Porphyrin. *J. Am. Chem. Soc.* **139**, 14129–14136 (2017).
50. Bischoff, F. *et al.* Metalation of Porphyrins by Lanthanide Atoms at Interfaces: Direct Observation and Stimulation of Cerium Coordination to 2H-TPP/Ag(111). *J. Phys. Chem. C* **122**, 5083–5092 (2018).
51. Cirera, B., Gallego, J. M., Martínez, J. I., Miranda, R. & Écija, D. Lanthanide-porphyrin species as Kondo irreversible switches through tip-induced coordination chemistry. *Nanoscale* **13**, 8600–8606 (2021).
52. Gottfried, J. M. Surface chemistry of porphyrins and phthalocyanines. *Surface Science Reports* vol. 70 259–379 (2015).
53. Écija, D. *et al.* Assembly and manipulation of rotatable cerium porphyrinato sandwich complexes on a surface. *Angew. Chemie - Int. Ed.* **50**, 3872–3877 (2011).
54. Diller, K. *et al.* Magnetic properties of on-surface synthesized single-ion molecular magnets. *RSC Adv.* **9**, 34421–34429 (2019).
55. Urgel, J. I. *et al.* In-Situ Growth of Gadolinium Phthalocyaninato Sandwich Complexes on the Ag(111) Surface. *ChemPhysChem* **20**, 2301–2304 (2019).
56. Isshiki, H. *et al.* Scanning tunneling microscopy investigation of Tris(phthalocyaninato) yttrium triple-decker molecules deposited on Au(111). *J. Phys. Chem. C* **114**, 12202–12206 (2010).
57. Deng, Z. *et al.* Self-assembly of bis(phthalocyaninato)terbium on metal surfaces. *Phys. Scr.* **90**, (2015).
58. Gonidec, M. *et al.* Surface supramolecular organization of a terbium(III) double-decker complex on graphite and its single molecule magnet behavior. *J. Am. Chem. Soc.* **133**, 6603–6612 (2011).
59. Stepanow, S. *et al.* Spin and orbital magnetic moment anisotropies of monodispersed bis(Phthalocyaninato)terbium on a copper surface. *J. Am. Chem. Soc.* **132**, 11900–11901 (2010).
60. Margheriti, L. *et al.* X-Ray Detected Magnetic Hysteresis of Thermally Evaporated Terbium Double-Decker Oriented Films. *Adv. Mater.* **22**, 5488–5493 (2010).
61. Gonidec, M., Davies, E. S., McMaster, J., Amabilino, D. B. & Veciana, J. Probing the magnetic properties of three interconvertible redox states of a single-molecule magnet with magnetic circular dichroism spectroscopy. *J. Am. Chem. Soc.* **132**, 1756–1757 (2010).
62. Cirera, B. *et al.* Preservation of electronic properties of double-decker complexes on metallic supports. *Phys. Chem. Chem. Phys.* **19**, 8282–8287 (2017).
63. Studniarek, M. *et al.* Understanding the Superior Stability of Single-Molecule Magnets on an Oxide Film. *Adv. Sci.* **6**, 1901736 (2019).
64. Donati, F. *et al.* Magnetic remanence in single atoms. *Science (80-.).* **352**, 318–321 (2016).
65. Malavolti, L. *et al.* Magnetism of TbPc2 SMMs on ferromagnetic electrodes used in organic spintronics. *Chem. Commun.* **49**, 11506–11508 (2013).
66. Serrano, G. *et al.* Magnetic bistability of a TbPc2 submonolayer on a graphene/SiC(0001) conductive electrode. *Nanoscale* **10**, 2715–2720 (2018).
67. Marocchi, S. *et al.* Relay-Like Exchange Mechanism through a Spin Radical between TbPc2 Molecules and Graphene/Ni(111) Substrates. *ACS Nano* **10**, 9353–9360 (2016).
68. Liu, F. *et al.* Single-Electron Lanthanide-Lanthanide Bonds Inside Fullerenes toward Robust Redox-Active Molecular

Magnets. *Acc. Chem. Res.* **52**, 2981–2993 (2019).
69. Westerström, R. *et al.* An endohedral single-molecule magnet with long relaxation times: DySc 2N@C 80. *J. Am. Chem. Soc.* **134**, 9840–9843 (2012).
70. Velkos, G. *et al.* High Blocking Temperature of Magnetization and Giant Coercivity in the Azafullerene Tb2@C79N with a Single-Electron Terbium–Terbium Bond. *Angew. Chemie Int. Ed.* **58**, 5891–5896 (2019).
71. Paschke, F. *et al.* Exceptionally High Blocking Temperature of 17 K in a Surface-Supported Molecular Magnet. *Adv. Mater.* **33**, 2102844 (2021).
72. Krylov, D. S. *et al.* Substrate-Independent Magnetic Bistability in Monolayers of the Single-Molecule Magnet Dy 2 ScN@C 80 on Metals and Insulators. *Angew. Chemie Int. Ed.* **59**, 5756–5764 (2020).
73. Dreiser, J. *et al.* Out-of-Plane Alignment of Er(trensal) Easy Magnetization Axes Using Graphene. *ACS Nano* **10**, 2887–2892 (2016).
74. Lucaccini, E., Sorace, L., Perfetti, M., Costes, J. P. & Sessoli, R. Beyond the anisotropy barrier: slow relaxation of the magnetization in both easy-axis and easy-plane Ln(trensal) complexes. *Chem. Commun.* **50**, 1648–1651 (2014).
75. Pedersen, K. S. *et al.* Modifying the properties of 4f single-ion magnets by peripheral ligand functionalisation. *Chem. Sci.* **5**, 1650–1660 (2014).
76. Donati, F. & Heinrich, A. J. A perspective on surface-adsorbed single atom magnets as atomic-scale magnetic memory. *Appl. Phys. Lett.* **119**, 160503 (2021).
77. Pivetta, M., Pacchioni, G. E., Schlickum, U., Barth, J. V. & Brune, H. Formation of Fe cluster superlattice in a metal-organic quantum-box network. *Phys. Rev. Lett.* **110**, (2013).
78. Sessoli, R. Single-atom data storage. *Nature* **543**, 189–190 (2017).
79. Natterer, F. D. *et al.* Reading and writing single-atom magnets. *Nature* **543**, 226–228 (2017).
80. Singha, A. *et al.* 4f occupancy and magnetism of rare-earth atoms adsorbed on metal substrates. *Phys. Rev. B* **96**, 224418 (2017).
81. Baltic, R. *et al.* Magnetic properties of single rare-earth atoms on graphene/Ir(111). *Phys. Rev. B* **98**, (2018).
82. Donati, F. *et al.* Correlation between Electronic Configuration and Magnetic Stability in Dysprosium Single Atom Magnets. *Nano Lett.* (2021) doi:10.1021/ACS.NANOLETT.1C02744.
83. Singha, A. *et al.* Engineering atomic-scale magnetic fields by dysprosium single atom magnets. *Nat. Commun.* **12**, 1–6 (2021).
84. Gallego, J. M. Substrate-Mediated Interactions. *Encycl. Interfacial Chem. Surf. Sci. Electrochem.* 166–174 (2018) doi:10.1016/B978-0-12-409547-2.13019-7.
85. Silly, F. *et al.* Creation of an Atomic Superlattice by Immersing Metallic Adatoms in a Two-Dimensional Electron Sea. *Phys. Rev. Lett.* **92**, 4 (2004).
86. Cao, R. X. *et al.* Self-organized Gd atomic superlattice on Ag(111): Scanning tunneling microscopy and kinetic Monte Carlo simulations. *Surf. Sci.* **610**, 65–69 (2013).
87. Donati, F. *et al.* Magnetic remanence in single atoms. *Science (80-.).* **352**, 318–321 (2016).
88. Pivetta, M., Rusponi, S. & Brune, H. Direct capture and electrostatic repulsion in the self-assembly of rare-earth atom superlattices on graphene. *Phys. Rev. B* **98**, (2018).
89. Natterer, F. D., Donati, F., Patthey, F. & Brune, H. Thermal and Magnetic-Field Stability of Holmium Single-Atom Magnets. *Phys. Rev. Lett.* **121**, 027201 (2018).
90. Baltic, R. *et al.* Superlattice of Single Atom Magnets on Graphene. *Nano Lett.* **16**, 7610–7615 (2016).
91. Furukawa, H., Cordova, K. E., O'Keeffe, M. & Yaghi, O. M. The chemistry and applications of metal-organic frameworks. *Science (80-.).* **341**, (2013).
92. Barth, J. V. Fresh perspectives for surface coordination chemistry. *Surf. Sci.* **603**, 1533–1541 (2009).
93. Hmadeh, M. *et al.* New Porous Crystals of Extended Metal-Catecholates. *Chem. Mater.* **24**, 3511–3513 (2012).
94. Dong, L., Gao, Z. A. & Lin, N. Self-assembly of metal–organic coordination structures on surfaces. *Prog. Surf. Sci.* **91**, 101–135 (2016).
95. Écija, D. *et al.* Five-vertex Archimedean surface tessellation by lanthanide-directed molecular self-assembly. *Proc. Natl. Acad. Sci. U. S. A.* **110**, 6678–6681 (2013).
96. Urgel, J. I. *et al.* Five-Vertex Lanthanide Coordination on Surfaces: A Route to Sophisticated Nanoarchitectures and Tessellations. *J. Phys. Chem. C* **118**, 12908–12915 (2014).
97. Urgel, J. I. *et al.* Quasicrystallinity expressed in two-dimensional coordination networks. *Nat. Chem.* **8**, 657–662 (2016).
98. Urgel, J. I. *et al.* Orthogonal Insertion of Lanthanide and Transition-Metal Atoms in Metal-Organic Networks on Surfaces. *Angew. Chemie* **127**, 6261–6265 (2015).
99. Lyu, G. *et al.* Tunable lanthanide-directed metallosupramolecular networks by exploiting coordinative flexibility through ligand stoichiometry. *Chem. Commun.* **52**, 1618–1621 (2016).
100. Urgel, J. I. *et al.* Surface-Supported Robust 2D Lanthanide-Carboxylate Coordination Networks. *Small* **11**, 6358–6364 (2015).
101. Cirera, B. *et al.* Dysprosium-carboxylate nanomeshes with tunable cavity size and assembly motif through ionic interactions. *Chem. Commun.* **52**, 11227–11230 (2016).
102. Uphoff, M. *et al.* Assembly of Robust Holmium-Directed 2D Metal–Organic Coordination Complexes and Networks on the Ag(100) Surface. *ACS Nano* **12**, 11552–11560 (2018).
103. Liu, J. *et al.* On-surface preparation of coordinated lanthanide-transition-metal clusters. *Nat. Commun.* **12**, 1–10 (2021).
104. Moreno Cerrada, D. *et al.* Stoichiometry-Directed Two-Level Hierarchical Growth of Lanthanide-Based Supramolecular Nanoarchitectures. *Chem. – A Eur. J.* e202300461 (2023) doi:10.1002/CHEM.202300461.
105. Parreiras, S. O. *et al.* Tuning the Magnetic Anisotropy of Lanthanides on a Metal Substrate by Metal–Organic Coordination. *Small* **17**, 2102753 (2021).
106. Moreno, D. *et al.* Engineering Periodic Dinuclear Lanthanide-Directed Networks Featuring Tunable Energy Level Alignment and Magnetic Anisotropy by Metal

Exchange. *Small* 2107073 (2022) doi:10.1002/SMLL.202107073.
107. Parreiras, S. O. *et al.* Lanthanide metal-organic network featuring strong perpendicular magnetic anisotropy. *Nanoscale* (2023) doi:10.1039/d2nr07189d.
108. Liu, K. *et al.* Constraining the coordination geometries of lanthanide centers and magnetic building blocks in frameworks: a new strategy for molecular nanomagnets. *Chem. Soc. Rev.* **45**, 2423–2439 (2016).
109. Biswas, S. & Neugebauer, P. Lanthanide-Based Metal-Organic-Frameworks for Proton Conduction and Magnetic Properties. *Eur. J. Inorg. Chem.* **2021**, 4610–4618 (2021).
110. Thorarinsdottir, A. E. & Harris, T. D. Metal-Organic Framework Magnets. *Chemical Reviews* vol. 120 8716–8789 (2020).
111. de Miguel, J. J. *et al.* Influence of the growth conditions on the magnetic properties of fcc cobalt films: from monolayers to superlattices. *J. Magn. Magn. Mater.* **93**, 1–9 (1991).
112. Corradini, V. *et al.* Probing magnetic coupling between LnPc2 (Ln = Tb, Er) molecules and the graphene/Ni (111) substrate with and without Au-intercalation: Role of the dipolar field. *Nanoscale* **10**, 277–283 (2018).
113. Huttmann, F. *et al.* Europium Cyclooctatetraene Nanowire Carpets: A Low-Dimensional, Organometallic, and Ferromagnetic Insulator. *J. Phys. Chem. Lett.* **10**, 911–917 (2019).
114. Huttmann, F., Schleheck, N., Atodiresei, N. & Michely, T. On-Surface Synthesis of Sandwich Molecular Nanowires on Graphene. *J. Am. Chem. Soc.* **139**, 9895–9900 (2017).
115. Wang, H., Wang, K., Tao, J. & Jiang, J. Twist angle perturbation on mixed (phthalocyaninato)(porphyrinato) dysprosium(III) double-decker SMMs. *Chem. Commun.* **48**, 2973–2975 (2012).
116. Cucinotta, G. *et al.* Magnetic anisotropy in a dysprosium/DOTA single-molecule magnet: Beyond simple magneto-structural correlations. *Angew. Chemie - Int. Ed.* **51**, 1606–1610 (2012).
117. Murugesu, M. The orientation is in the details. *Nat. Chem.* **4**, 347–348 (2012).
118. Thole, B. T., Carra, P., Sette, F. & Van Der Laan, G. X-ray circular dichroism as a probe of orbital magnetization. *Phys. Rev. Lett.* **68**, 1943–1946 (1992).
119. Carra, P., König, H., Thole, B. T. & Altarelli, M. Magnetic X-ray dichroism. General features of dipolar and quadrupolar spectra. *Phys. B Phys. Condens. Matter* **192**, 182–190 (1993).
120. Moreno, D. *et al.* Dysprosium-directed metallosupramolecular network on graphene/Ir(111). *Chem. Commun.* **57**, 1380–1383 (2021).
121. Heinrich, A. J. *et al.* Quantum-coherent nanoscience. *Nat. Nanotechnol. 2021 1612* **16**, 1318–1329 (2021).
122. Chen, Y., Bae, Y. & Heinrich, A. J. Harnessing the Quantum Behavior of Spins on Surfaces. *Adv. Mater.* 2107534 (2022) doi:10.1002/ADMA.202107534.
123. Liddle, S. T. & Van Slageren, J. Improving f-element single molecule magnets. *Chem. Soc. Rev.* **44**, 6655–6669 (2015).
124. Bartolomé, E., Arauzo, A., Luzón, J., Bartolomé, J. & Bartolomé, F. Magnetic Relaxation of Lanthanide-Based Molecular Magnets. in *Handbook of Magnetic Materials* vol. 26 1–289 (Elsevier, 2017).
125. Bar, A. K., Kalita, P., Singh, M. K., Rajaraman, G. & Chandrasekhar, V. Low-coordinate mononuclear lanthanide complexes as molecular nanomagnets. *Coordination Chemistry Reviews* vol. 367 163–216 (2018).